


Bénard–von Kármán vortex street in a spin-orbit-coupled Bose-Einstein condensateXue-Ying Yang ^{1,2} Xiao-Lin Li,^{1,2} Na Tang,^{1,2} Zhi-Kun Zhou,^{1,2} Lin Song,^{1,2} Juan Zhang,^{1,2,3} and Yu-Ren Shi^{1,2,*}¹College of Physics and Electronic Engineering, Northwest Normal University, Lanzhou 730070, People's Republic of China²Key Laboratory of Atomic and Molecular Physics and Functional Materials of Gansu Province, Lanzhou 730070, People's Republic of China³Department of Basic Courses, Lanzhou Institute of Technology, Lanzhou 730070, People's Republic of China

(Received 11 November 2019; accepted 2 September 2020; published 18 September 2020; corrected 22 September 2020)

The dynamics of pseudo-spin-1/2 Bose-Einstein condensates with weak spin-orbit coupling through a moving obstacle potential are studied numerically. Four types of wakes are observed and the phase diagrams are determined for different spin-orbit coupling strengths. The conditions to form Bénard–von Kármán vortex street are rather rigorous, and we investigate in detail the dynamical characteristics of the vortex streets. The two point vortices in a pair rotate around their center, and the angular velocity and their distance oscillate periodically. The oscillation intensifies with increasing spin-orbit coupling strengths, and it makes part of the vortex pairs dissociate into separate vortices or combine into single ones and destroys the vortex street in the end. The width b of the street and the distance l between two consecutive vortex pairs of the same circulation are determined by the potential radius and its moving velocity, respectively. The b/l ratios are independent of the spin-orbit coupling strength and fall in the range 0.19–0.27, which is a little smaller than the stability criterion 0.28 for classical fluids. Proper b/l ratios are necessary to form Bénard–von Kármán vortex street, but the spin-orbit coupling strength affects the stability of the street patterns. Finally, we propose a protocol to experimentally realize the vortex street in ⁸⁷Rb spin-orbit-coupling Bose-Einstein condensates.

DOI: [10.1103/PhysRevE.102.032217](https://doi.org/10.1103/PhysRevE.102.032217)**I. INTRODUCTION**

When an obstacle potential moves at proper conditions, a series of vortices will shed alternately at the two sides of the wake. This phenomenon is known as Bénard–von Kármán (BvK) vortex street [1–7] and it is common in classical fluids. When the BvK vortex street occurs, the fluid produces periodically alternating lateral forces on the object. If the frequency of the forces is close to the natural frequency of the object, it will cause resonance and even damage the object. Bose-Einstein condensates (BECs) are ideal test bed for studying vortex street because they can provide direct insight into the onset of the turbulence [8–11]. So they have aroused great interest both in experimental and theoretical studies. Numerical simulations on the quasi-two-dimensional (2D) scalar BECs show that the BvK vortex street is observed in the wake when the velocities have appropriate values while the turbulent flow are generated by strong perturbation of the obstacle at high velocities [9]. Quantum vortex shedding in high flat-rate BEC was experimentally studied in 2016, and regular shedding of the vortex pairs with same sign was observed [12]. Hiroki *et al.* investigated numerically the dynamics of an exciton-polariton superfluid and they found that the BvK vortex street is generated in the wake behind an obstacle potential [13].

Lin *et al.* had created a spin-orbit-coupled BECs with two spin states of ⁸⁷Rb in an experiment [14]. The success-

ful realization of SOC BECs has attracted a lot attention in the past decade, and many theoretical modes were proposed [15–23]. Artificial SOC BEC offers more opportunities to explore novel quantum states because of the coupling of the internal spin states and the centroid operation [24–30]. To the best of our knowledge, there is no experimental or theoretical investigations about BvK vortex street in SOC BECs, and we wonder how SOC affects the stability of the vortex street.

In this paper, we explore the dynamical properties of SOC BEC with a moving obstacle by using the time-splitting Fourier spectral method. Different types of wakes such as vortex-antivortex pairs and BvK vortex street are observed. In order to determine the parameter ranges corresponding to different wakes, systematical simulations are performed for different SOC strengths κ , potential radii d , and velocities v . The ratio of the width of the street to the distance between two consecutive vortex pairs in one array is calculated to characterize the stability of vortex street. The angular velocity and distance of the two point vortices in a pair are calculated at different SOC strengths κ . In addition, the drag force generated along with the vortex shedding is calculated, and the physical mechanisms for different wake distributions are analyzed. The paper is organized as follows: Sec. II formulates the theoretical model for SOC BECs with a moving obstacle potential. In Sec. III, we determine the phase diagrams that show wake distribution patterns at different SOC strengths and potential parameters. Section IV summarizes the main results.

*shiy@nwnu.edu.cn

II. THEORETICAL METHOD

The Hamiltonian of a BEC with SOC can be written in the Gross-Pitaevskii (GP) form [30]

$$\begin{aligned} H = & \int d\vec{r} \bar{\Psi}^\dagger \left(\frac{\vec{p}^2}{2m} + V_{\text{op}} - \frac{\hbar^2 k_0}{m} \vec{p} \cdot \sigma_\perp \right) \bar{\Psi} \\ & + \int d\vec{r} \left(\sum_{j=\uparrow, \downarrow} \frac{g_{jj}}{2} |\psi_j|^4 + g_{\uparrow\downarrow} |\psi_\uparrow|^2 |\psi_\downarrow|^2 \right), \end{aligned} \quad (1)$$

where m is the atomic mass, k_0 is the SOC strength, $\sigma_\perp = (\sigma_x, \sigma_y)$ are the 2×2 Pauli matrices, and $g_{jl} = 4\pi \hbar^2 a_{jl}/m$ with $a_{jl} = a_{lj}$ ($j, l = \uparrow, \downarrow$) being the s-wave scattering lengths between the j th and l th components. V_{op} is the obstacle potential. The wave function $\bar{\Psi}(\vec{r}) = [\psi_\uparrow(\vec{r}), \psi_\downarrow(\vec{r})]^T$, and the superscript T denotes transposition. The total number of the particles are $N = \int |\bar{\Psi}|^2 d\vec{r}$.

In experiments, BEC is usually confined in a harmonic potential. When the trap is strongly anisotropic ($\omega_z \gg \omega_x, \omega_y$), BEC will be disk-shaped in the xy plane. Thus, the dynamic behaviors of the BEC can be described by a set of quasi-2D GP equation (GPE) within the approximation of mean-field theory [31]. In this work, we consider a quasi-2D spin-1/2 BEC with Rashba spin-orbit coupling (SOC), in which an obstacle potential is moving. In the following, we normalize the length and time by the healing length $a_0 = \sqrt{\hbar/m\omega_0}$ and the characteristic time $1/\omega_0$ with $\omega_0 = \min(\omega_x, \omega_y)$, under which $E \rightarrow E/(\hbar\omega_0)$, $\psi \rightarrow \psi/\sqrt{n_0 m \omega_0 / \hbar}$, $g_{jl} \rightarrow g_{jl} m n_0 / (l_z \hbar^2 \sqrt{2\pi})$, where $l_z = \sqrt{\hbar/m\omega_z}$, and n_0 is the given particle density. The dimensionless coupled GPE read

$$\begin{aligned} i\partial_t \psi_\uparrow &= [-1/2\nabla^2 + V_{\text{op}} + i\kappa\partial_- + g_{\uparrow\uparrow} |\psi_\uparrow|^2 + g_{\uparrow\downarrow} |\psi_\downarrow|^2] \psi_\uparrow, \\ i\partial_t \psi_\downarrow &= [-1/2\nabla^2 + V_{\text{op}} + i\kappa\partial_+ + g_{\downarrow\downarrow} |\psi_\downarrow|^2 + g_{\downarrow\uparrow} |\psi_\uparrow|^2] \psi_\downarrow, \end{aligned} \quad (2)$$

where $\kappa = k_0 \sqrt{\hbar/m\omega_0}$, $\partial_\pm = \partial/\partial x \pm i\partial/\partial y$. The ground state is the plane-wave state for $g_{\uparrow\downarrow}/g_{\uparrow\uparrow} < 1$ and the stripe state for $g_{\uparrow\downarrow}/g_{\uparrow\uparrow} > 1$, which breaks the rotational symmetry of the system [32].

We numerically solve Eq. (2) by the Fourier spectral method [33] under periodic boundary conditions. The initial state uses the ground state, and it is obtained by the imaginary-time propagation method with a zero potential velocity [34]. When the nonlinear dynamical evolution is performed, the obstacle potential is assumed moving at a constant velocity v . At the beginning of computation, small random disturbance is added on the ground state to break the symmetry of the system. The computational domain is taken to be $256a_0 \times 64a_0$, and steady inflow-outflow boundary conditions are used to deal with the vortices by ‘‘recycling’’ flow in a periodic domain [35].

III. NUMERICAL RESULTS

Now we employ a Gaussian potential with peak strength V_0 and radius d of the form

$$V_{\text{op}} = V_0 e^{-\frac{(x-x_0+vt)^2 + y^2}{d^2}},$$

which moves along the $-x$ direction from the initial position x_0 . Figure 1 shows the density and phase distribution of the BEC wakes caused by the obstacle potential. From Figs. 1(a) and 1(e), it is clear that quantum vortices cannot be excited when the obstacle potential moves at low velocities or its radius is small. It indicates, according to the d’Alembert paradox, that a stable velocity field can be created in a dissipationless system.

In ordinary perfect fluids, it is well known that a shock begins to form when the velocity reaches a critical value. In BECs, however, the shock waves are replaced by the generation of vortices due to the absence of intrinsic molecular damping. The generation of vortices leads to a vortical dissipative flow on a large scale. When the velocity has appropriate values, a pair of vortex-antivortex will be emitted as shown in Figs. 1(b) and 1(f), and they have opposite circulations $\pm h/m$. When the vortex-antivortex pair is shed, the velocity field of the vortices balances the velocities behind the obstacle potential, which makes the local velocities smaller than the critical velocity. After the vortex pair leaves the obstacle for a distance, its contributions to the velocity around the obstacle weaken and the total velocity becomes greater than the critical value again, and a new vortex pair is generated. The rotation of the vortices obey $\dots(+)(-)(+)(-)\dots$, where $+$ and $-$ indicate the clockwise and counterclockwise circulations. The line between the two vortex centers in a pair keeps perpendicular to the moving direction of the pair. Eventually, the emitted vortex pairs evolve into a V-shaped wake, as shown in Fig. 1(b).

When the obstacle potential moves with larger velocities, BvK vortex street appears [Figs. 1(c) and 1(g)]. Similar to the scalar BEC, two point vortices with same circulation h/m form a pair. A series of clockwise and counterclockwise pairs are shed alternately. After the vortex pair is shed, the two vortices rotate around their center while they move along the $-x$ direction, and the translation velocity oscillates slightly. The average velocity of the vortex pairs is $\tilde{v}_n \simeq 0.66\sqrt{\hbar\omega_0/m} \simeq 0.044$ mm/s. The average distance between two rows of the vortex street is $b = 4.39a_0$, and the distance between two neighbor pairs in the same row is $l = 20.33a_0$. The ratio b/l is 0.22, which is a little smaller than the stability condition $b/l = \pi^{-1} \cosh^{-1} \sqrt{2} \approx 0.28$ of the classical Kármán vortex street. The translation velocity can also be obtained theoretically by $\tilde{v}_t = h/(\sqrt{2}lm)$, which gives 0.042 mm/s. It can be seen that the numerical result is consistent well with the theoretical prediction. With increasing of the obstacle velocity, the emission of the vortices becomes more irregular, as shown in Figs. 1(d) and 1(h). For all of the cases in Fig. 1, the profiles of wave functions $\psi_\downarrow(r)$ are omitted because they are similar to $\psi_\uparrow(r)$.

The phase diagram for different values of d and v at the SOC strengths $\kappa = 0.01, 0.03, 0.06,$ and 0.09 is obtained by performing systematical simulations. The regions I–IV in Fig. 2 correspond to the four types of the wakes in Fig. 1, that is, the steady laminar flow, the vortex pair, BvK vortex street, and irregular turbulence. Figure 2(a) is for the SOC strength $\kappa = 0.01$, and the BvK vortex streets generate when $0.8a_0 < d < 1.6a_0$ and $0.64\sqrt{\hbar\omega_0/m} < v < 0.78\sqrt{\hbar\omega_0/m}$. For $\kappa = 0.03$, the region to form BvK vortex streets decreases slightly. Steady vortex streets occur at the parameters

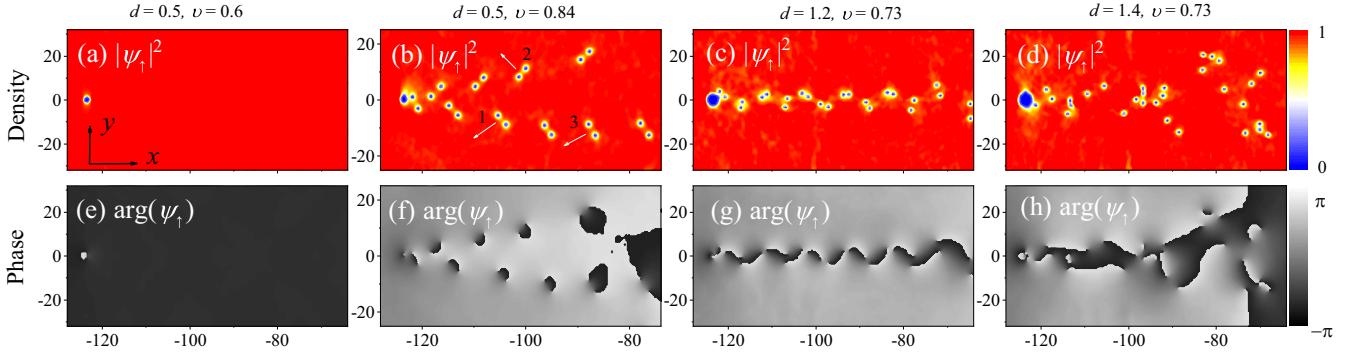


FIG. 1. Density $|\psi_{\uparrow}|^2$ (upper panel) and phase (lower panel) distributions of condensates with an obstacle potential for different radius d and velocity v . (a) No vortex at $(d, v) = (0.5, 0.60)$. (b) V-shaped vortex pairs at $(d, v) = (0.5, 0.84)$. (c) BvK vortex street at $(d, v) = (1.2, 0.73)$. (d) Irregular at $(d, v) = (1.4, 0.73)$. The white arrows in panel (b) indicate the directions that the vortex-antivortex pairs move. The dimensionless intra- and intercomponent interaction coefficients are $g_{\uparrow\uparrow} = 1$, $g_{\uparrow\downarrow} = 0.9$. SOC strength $\kappa = 0.01$. The density is normalized by n_0 . The view of field is $64a_0 \times 64a_0$. The computational domain is taken to be $256a_0 \times 64a_0$, and the obstacle potential begin moving at $x = -16a_0$ along the $-x$ direction.

$0.9a_0 < d < 1.5a_0$ and $0.64\sqrt{\hbar\omega_0/m} < v < 0.76\sqrt{\hbar\omega_0/m}$, as shown in Fig. 2(b). When κ increases further to 0.06, the conditions for generating the BvK vortex street gets quite restricted; it appears only in a small parameter region $1.1a_0 < d < 1.3a_0$ and $0.66\sqrt{\hbar\omega_0/m} < v < 0.68\sqrt{\hbar\omega_0/m}$. When κ increases to 0.09, steady BvK vortex streets are not observed

in the parameter range of our simulations. However, vortex street structures with short lives appear at the area marked by \times in Fig. 2(d). In fact, in the regions near the boundaries of the steady vortex street [outside of the solid white lines in Figs. 2(b) and 2(c)], paroxysmal vortex streets appear but they cannot exist for a long time. Examples of the paroxysmal

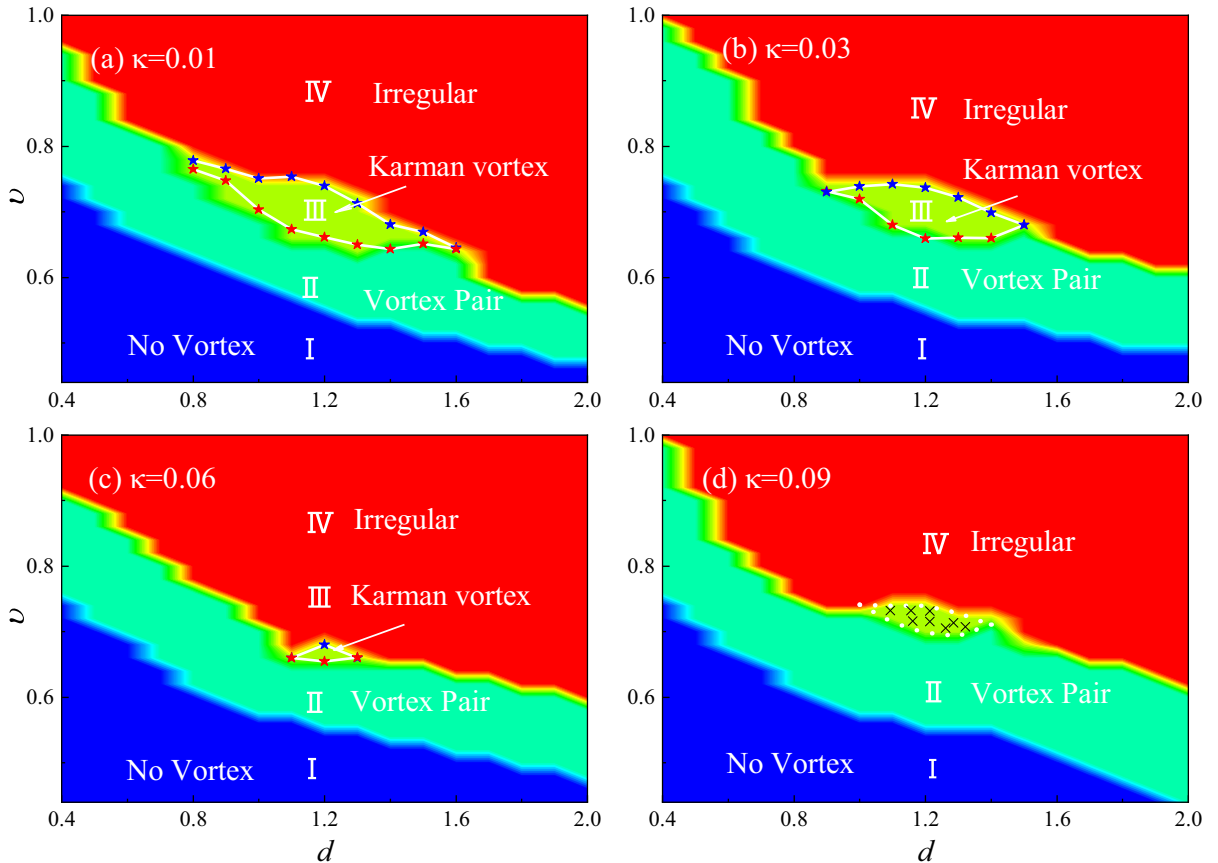


FIG. 2. Dependence of the patterns of wakes on the SOC strength κ , radius d , and velocity v of the obstacle potential. The I–IV regions correspond to the flow patterns shown in Figs. 1(a)–1(d), respectively. The dimensionless intra- and intercomponent interaction coefficients are $g_{\uparrow\uparrow} = 1$, $g_{\uparrow\downarrow} = 0.9$. SOC strength κ is 0.01, 0.03, 0.06, and 0.09, respectively. The area surrounded by white solid lines is the range of vortex streets.

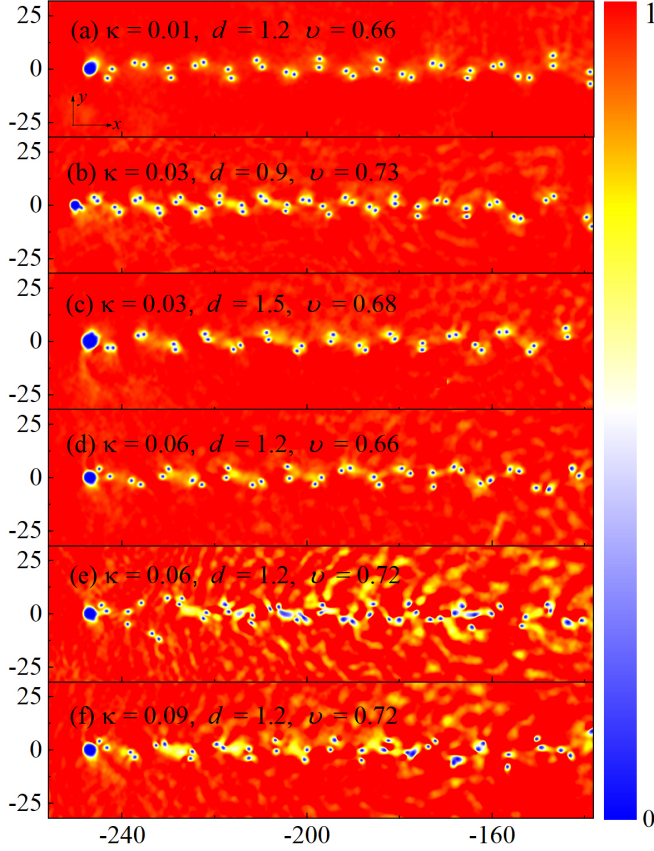


FIG. 3. Density distribution $|\psi_{\uparrow}|^2$ of condensates with different SOC strength κ , radii d , and velocities v . $g_{\uparrow\uparrow} = 1$, $g_{\uparrow\downarrow} = 0.9$. The field of view is $128a_0 \times 64a_0$. (a) $\kappa = 0.01$, $d = 1.2$, $v = 0.66$. (b) $\kappa = 0.03$, $d = 0.9$, $v = 0.73$. (c) $\kappa = 0.03$, $d = 1.5$, $v = 0.68$. (d) $\kappa = 0.06$, $d = 1.2$, $v = 0.66$. (e) $\kappa = 0.06$, $d = 1.2$, $v = 0.72$. (f) $\kappa = 0.09$, $d = 1.2$, $v = 0.72$.

vortex streets are illustrated in Fig. 3(e). The above results suggest that increasing SOC strengths weakens the stability of the vortex pairs, and it eventually destroys the formation of the von Kármán vortex street.

Compared with other phases, the conditions to form BvK vortex street are rather rigorous. Previous studies on scalar BEC show that smaller obstacles tend to shed the vortex pairs and larger ones tend to generate vortex streets [9]. The vortex pairs appear in all of the diameters in our simulations; however, BvK vortex street occurs only for some potential diameters with combination of proper velocities. The discrepancies suggest that the dynamic characteristics of the quantized vortices are changed dramatically by the coupling between spin and orbital motion degrees of freedom, and it explains why the BvK vortex street is difficult to observe experimentally for SOC BEC.

To offer more details for the dynamic evolutions and the dependence of the vortex structures on different parameters, typical diagrams of BvK vortex street are illustrated in Fig. 3. At weak SOC strengths, the structure of vortex street as shown in Fig. 3(a) can exist for a long time, and no paroxysmal vortex street is observed. For $\kappa = 0.03$, stable vortex streets can exist for a long time for the parameters in region III of Fig. 2(b). Figures 3(b) and 3(c) show the vortex streets

TABLE I. The ratio of the width b of the vortex street to the distance l between two consecutive vortex pairs in one array at different parameters.

κ	d	v	b	l	b/l
0.01	1.2	0.66	5.0	26.0	0.19
0.03	0.9	0.73	4.5	17.9	0.25
0.03	1.2	0.73	5.0	18.5	0.27
0.03	1.2	0.68	5.0	24.6	0.20
0.03	1.5	0.68	5.8	27.4	0.21
0.06	1.2	0.66	5.3	26.2	0.20

generated at $d = 0.9a_0$ (the left end) and $d = 1.5a_0$ (the right end). Short-lived vortex street structures can be observed at smaller $d = 0.7a_0$ and larger $d = 1.7a_0$. When κ increases to 0.06, long-term stable vortex streets can be observed only in a quite small region as shown in Fig. 2(c), but short-lived vortex streets occur at similar parameter ranges as given in Fig. 2(b) (for the d values in $0.8a_0$ – $1.8a_0$). Figures 3(d) and 3(e) show the dynamic evolution of the wakes generated at $d = 1.2a_0$ with the velocities $v = 0.66\sqrt{\hbar\omega_0/m}$ (at the lower boundary) and $v = 0.72\sqrt{\hbar\omega_0/m}$ (above the upper boundary). The structure of the vortex street is comparatively stable in Fig. 3(e) when the obstacle potential moves from $x = -120a_0$ to $x = -220a_0$. In the wakes close to the obstacle potential, “V-shaped” vortex pairs are formed. When the SOC strength reaches 0.09, it is hard to observe steady vortex street. Figure 3(f) shows the wakes at $d = 1.2a_0$ and $v = 0.72\sqrt{\hbar\omega_0/m}$ for $\kappa = 0.09$. The vortex pairs shed from the obstacle still form vortex street, and the edges of the point vortices are clear for some limited time. As the time goes on, part of the vortex pairs may merge into single-point vortices, and they gradually evolve into disordered states. This means that increasing κ affects not only the distributions of vortex pairs but also the stability of the point vortices.

For classical fluids, the ratios of the width b of the street to the distance l between two consecutive vortex pairs in one array is an important criterion to the stability of BvK vortex street, and the b/l values should be close to 0.28. We calculate the b/l ratios for typical vortex streets formed at different conditions and the results are presented in Table I. For $\kappa = 0.03$, we choose four wakes at $d = 0.9a_0$ and $1.5a_0$ (left and right boundaries), and $d = 1.2a_0$ with $v = 0.68\sqrt{\hbar\omega_0/m}$ and $0.73\sqrt{\hbar\omega_0/m}$ (the lower and upper boundaries). It is found that the width b of the street is approximately proportional to the obstacle potential radius d . The distance l has a strong negative correlation with the velocity v of the obstacle and a weak positive correlation with the radius d . The b/l ratios are in the range 0.19 to 0.27 for stable BvK vortex streets. It is clear that the SOC strength κ does not affect the b/l ratios. In fact, we calculated the b/l ratios for all of the stable vortex streets, the b/l ratios fall in the range 0.19–0.27, and the values are generally around 0.22. It seems that b/l has larger values when the parameters are close to the upper boundaries. It is also noticed that the b/l values are about 0.22 for the vortex pairs generated in Fig. 3(f), but the structure of the vortex street can maintain only for a certain period of time and evolves eventually into irregular patterns. This implies that suitable b/l ratio is a necessary condition to form BvK

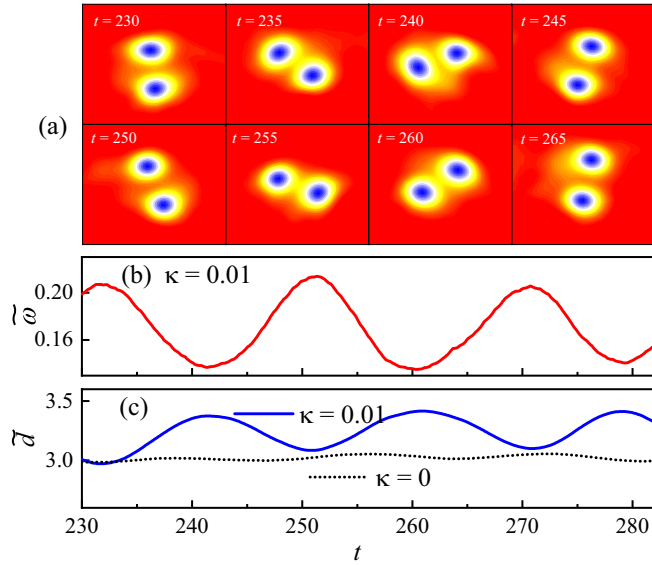


FIG. 4. (a) Contour plots of density $|\psi_\uparrow|^2$ centered at a specific pair of point vortices in Fig. 1(c). The view field is $10a_0 \times 10a_0$. (b) Angular velocity vs time t . (c) The distance between two point vortices vs time t . The physical parameters are the same as those in Fig. 1(c).

vortex street, but it cannot guarantee the stability of the vortex street. The stability conditions are not only related to the b/l ratios but also to the SOC strengths.

After the BvK vortex street is generated, the two vortices in a pair are shed from the same side of the obstacle and rotate with same circulation. So they rotate as a whole with the circulation opposite to the rotation of the individual vortices. Figure 4(a) shows a vortex pair that rotate counterclockwise. The physical parameters are the same as those in Fig. 1(c). The angular velocity ($\tilde{\omega}$) varies nearly periodically, as shown by Fig. 4(b), and the average angular velocity is 0.17. Figure 4(c) shows the distance \tilde{d} between two vortices in a pair. It is obtained by tracking the coordinates of two point vortices in the numerical simulations. It can be seen that \tilde{d} also changes periodically: The maximum distance corresponds to the minimum angular velocity at $t = 242\omega_0^{-1}$, and the minimum distance corresponds to the maximum angular velocity at $t = 251\omega_0^{-1}$. This is in accordance with the theoretical formula $\tilde{\omega} = 2\hbar/(m\tilde{d}^2)$ which says angular velocity $\tilde{\omega}$ is inversely proportional to the square of distance \tilde{d} . The black dotted line in Fig. 4(c) shows the distance \tilde{d} at $\kappa = 0$ and it keeps nearly constant. Previous studies by Sasaki *et al.* also showed that $\tilde{\omega}$ and \tilde{d} keep nearly constant in the scalar BEC [9].

The oscillation of the angular velocity $\tilde{\omega}$ and the distance \tilde{d} between two point vortices is a specific feature of the BvK vortex streets formed in SOC BECs. Figure 5 shows the time evolution of angular velocity $\tilde{\omega}$ and the distance \tilde{d} of the vortex pairs formed at different SOC strengths. The obstacle radius d and its moving velocity v are fixed to $1.2a_0$ and $0.66\sqrt{\hbar\omega_0/m}$. For $\kappa = 0.01, 0.03$, and 0.06 , the average distances \tilde{d} and their rms deviations are $2.98 \pm 0.08a_0$, $3.90 \pm 0.11a_0$, and $4.17 \pm 0.16a_0$, respectively. The corresponding angular velocity $\tilde{\omega}$ and their RMS deviations are

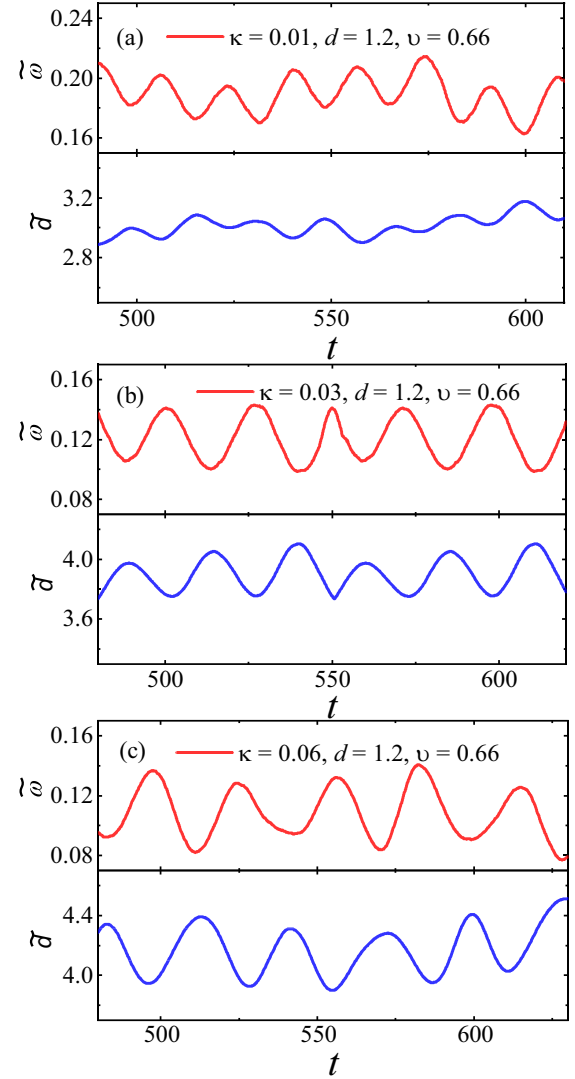


FIG. 5. Time evolution of the angular velocity and distance between two point vortices at different SOC strengths κ in the BvK vortex street. $g_{\uparrow} = 1, g_{\downarrow} = 0.9$.

$0.192 \pm 0.012\omega_0$, $0.120 \pm 0.014\omega_0$, and $0.108 \pm 0.017\omega_0$. It can be concluded that with increasing the SOC strength κ , the distances between two point vortices in a pair increase, and their oscillations intensify significantly. With larger κ , the rotation of the vortex pairs becomes slower, however, the fluctuations of the angular velocities get larger. Combined with the wake patterns described in Fig. 3, we can draw a picture about how the spin-orbital coupling affects the stability of the BvK vortex streets. The two point vortices in a pair vibrate, which enhances with increasing coupling strengths. The vibration makes some of the vortex pairs dissociate into separate vortices and some of them merge into single point vortices, and the BvK vortex streets are broken down in the end.

The emission of the vortices will cause a drag force $\vec{f} = (f_x, f_y) = \partial_t \int dx dy \vec{\Psi}^\dagger (i\hbar\nabla) \vec{\Psi}$. Figure 6 shows the time evolution of the drag forces at SOC strength $\kappa = 0.01$. The potential starts to move with velocity v at $t = 0$. Figure 6(a) corresponds to the dynamical behavior of V-shaped wake in Fig. 1(b). The f_x fluctuates irregularly at $t < 110\omega_0^{-1}$ and then

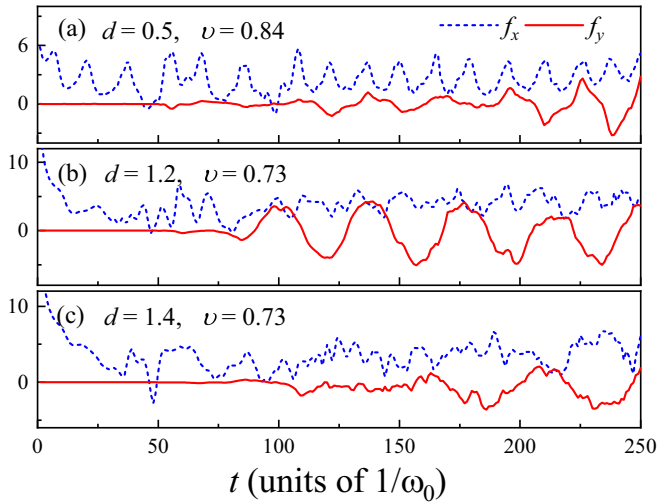


FIG. 6. Time evolution of the normalized drag force acted on the moving obstacle potential. The blue dashed and red solid lines show f_x and f_y , respectively. The parameters used in panels (a)–(c) are the same as those in Figs. 1(b)–1(d).

periodically. Each peak of f_x corresponds to the shedding of one vortex pair. When $t < 110\omega_0^{-1}$, f_y is nearly zero, indicating that the two vortices in a pair are shed simultaneously and keep perpendicular to the x axis and form a row. When $t > 110\omega_0^{-1}$, f_y begins oscillating, demonstrating that the vortex pairs start to incline after they are shed. Because of the asymmetry of the wakes, the vortices generated from the two sides of the obstacle emit at different time, and the V-shaped wake is formed at $t > 220\omega_0^{-1}$. The peaks and troughs of f_y represent the shedding of upper and lower vortex pairs, respectively, so the period of f_y is twice that of f_x . The above description shows that the periodic vortex generation can be understood as a process where the moving obstacle exerts a drag force and the accumulated energy is released as a vortex pair at a certain threshold condition. Figure 6(b) corresponds to the BvK vortex street in Fig. 1(c). At the beginning ($t < 85\omega_0^{-1}$), two point vortices with opposite circulations are shed from two sides of the obstacle. Then two vortices with same circulation are emitted from the same side of the obstacle, and clockwise and counterclockwise vortex pairs are shed alternately. The peaks of f_y corresponds to the shedding of clockwise pairs, and the troughs corresponds to the shedding of counterclockwise pairs. Figure 6(c) corresponds to irregular turbulence in Fig. 1(d). Although the wake patterns are not arranged regularly, f_y still oscillates periodically after the initial stage ($t > 160\omega_0^{-1}$). It suggests that clockwise and counterclockwise vortices are shed alternately. The oscillation period of f_y equals to the alternative shedding of the vortices from two sides of the obstacle. We also calculate the drag force at $\kappa = 0, 0.03, 0.09$. Compared with scalar BECs, SOC does not change the frequency and magnitude of the drag forces, and no essential differences are found.

Based on our simulations, we propose a scheme to realize the von Kármán vortex street in an experiment. The experiment can be performed with the apparatus described in Ref. [36]. We consider a ^{87}Rb SOC BEC in the pseudo-spin-up and -down states: $|\uparrow\rangle = |F = 1, m_F = 0\rangle$

and $|\downarrow\rangle = |F = 1, m_F = -1\rangle$. The number of atoms in the condensate is $N \approx 1.63 \times 10^6$. The condensate is confined in a harmonic trapping potential which is generated by combining a pancake-shaped optical dipole trap and a magnetic quadruple trap. The trapping frequencies $(\omega_x, \omega_y, \omega_z) \approx 2\pi \times (50, 50, 140)$ Hz [14], so the healing length $a_0 = \sqrt{\hbar/m\omega_x} \approx 3.81 \mu\text{m}$ and $l_z = \sqrt{\hbar/m\omega_z} \approx 2.27 \mu\text{m}$. The obstacle potential is formed by a repulsive Gaussian laser beam [12,35] moving at velocity $v = 0.14$ mm/s. Its peak strength $V_0 = 5.25 \times 10^{-31}$ J and the waist of beam $d = 4.57 \mu\text{m}$. The intra- and intercomponent interactions $g_{jl} = 4\pi\hbar^2 a_{jl}/m(j, l = \uparrow, \downarrow)$ can be tuned by the s -wave scattering length a_{jl} . Giving $a_{\uparrow\uparrow} = a_{\downarrow\downarrow} \approx 86a_B \approx 4.54$ nm and $a_{\uparrow\downarrow} = a_{\downarrow\uparrow} \approx 77a_B \approx 4.08$ nm (a_B is the Bohr radius), it leads to the values $g_{\uparrow\uparrow} = g_{\downarrow\downarrow} \approx 4.33 \times 10^{-51}$ J and $g_{\uparrow\downarrow} = g_{\downarrow\uparrow} \approx 3.90 \times 10^{-51}$ J. Under these conditions, the dimensionless intra- and intercomponent strengths are $g_{\uparrow\uparrow} \approx 1$ and $g_{\uparrow\downarrow} \approx 0.9$, so the parameters are close to Fig. 1(c) and von Kármán vortex street will be realized.

IV. CONCLUSION

In summary, we numerically simulate the dynamics of SOC BEC through a moving potential. Four kinds of wakes, namely, the stable laminar flow, vortex pairs, BvK vortex street, and irregular turbulence, are observed. The phase diagrams are determined for different SOC strengths κ . Compared with other phases, the conditions to form BvK vortex street are rather restricted, and the areas for the stable vortex streets reduce when the κ increases. We focus our attention on the dynamic characteristics of the vortex street. Increasing κ affects not only the distributions of vortex pairs, but also the stability of the point vortices. The values of the stability condition b/l range from 0.19 to 0.27 for the vortex streets in SOC BECs. It is a little smaller than that of the classical fluids. Suitable b/l ratio is a necessary condition to form the BvK vortex street, but it cannot guarantee the stability of the vortex street. The stability conditions are not only related to the b/l ratios but also to the SOC strengths. The two point vortices in a pair rotate around their center, and their distances and the angular velocities change periodically in the BvK vortex street. By increasing the SOC strength κ , the distances between two point vortices in a pair increase, and their oscillations intensify significantly. The vibration makes some of the vortex pairs dissociate into separate vortices, some of them merge into single point vortices, and the BvK vortex streets are broken down in the end. We calculate the drag forces and analyze the formation mechanism of different wake types. Compared with scalar BECs, SOC does not change the frequency and magnitude of the drag forces obviously. Finally, we propose a scheme to realize the vortex street in experiment.

ACKNOWLEDGMENT

This work is supported by the National Natural Science Foundation of China under Grants No. 11565021 and No. 12065022 and the Scientific Research Foundation of Northwest Normal University under Grant No. NWNULKQN-16-3.

- [1] S. Dong, G. S. Triantafyllou, and G. E. Karniadakis, *Phys. Rev. Lett.* **100**, 204501 (2008).
- [2] I. Kim and X. L. Wu, *Phys. Rev. E* **92**, 043011 (2015).
- [3] D. G. Crowdy and V. S. Krishnamurthy, *Phys. Rev. Fluids* **2**, 114701 (2017).
- [4] M. Iima, *Phys. Rev. E* **99**, 062203 (2019).
- [5] F. L. Ponta and H. Aref, *Phys. Rev. Lett.* **93**, 084501 (2004).
- [6] P. Boniface, L. Lebon, L. Limat, and M. Reueveur, *Europhys. Lett.* **117**, 34001 (2017).
- [7] B. Ahlborn, M. L. Seto, and B. R. Noack, *Fluid Dyn. Res.* **30**, 379 (2002).
- [8] M. J. Thoraval, K. Takehara, T. G. Etoh, S. Popinet, P. Ray, C. Josserand, S. Zaleski, and S. T. Thoroddsen, *Phys. Rev. Lett.* **108**, 264506 (2012).
- [9] K. Sasaki, N. Suzuki, and H. Saito, *Phys. Rev. Lett.* **104**, 150404 (2010).
- [10] G. W. Stagg, N. G. Parker, and C. F. Barenghi, *J. Phys. B: At. Mol. Opt. Phys.* **47**, 095304 (2014).
- [11] M. T. Reeves, T. P. Billam, B. P. Anderson, and A. S. Bradley, *Phys. Rev. Lett.* **114**, 155302 (2015).
- [12] W. J. Kwon, J. H. Kim, S. W. Seo, and Y. Shin, *Phys. Rev. Lett.* **117**, 245301 (2016).
- [13] H. Saito, T. Aioi, and T. Kadokura, *Phys. Rev. B* **86**, 014504 (2012).
- [14] Y. J. Lin, K. J. García, and I. B. Spielman, *Nature (London)* **471**, 83 (2011).
- [15] J. Ruseckas, G. Juzeliūnas, P. Öhberg, and M. Fleischhauer, *Phys. Rev. Lett.* **95**, 010404 (2005).
- [16] D. L. Campbell, G. Juzeliūnas, and I. B. Spielman, *Phys. Rev. A* **84**, 025602 (2011).
- [17] J. Y. Zhang, S. C. Ji, Z. Chen, L. Zhang, Z. D. Du, B. Yan, G. S. Pan, B. Zhao, Y. J. Deng, H. Zhai, S. Chen, and J. W. Pan, *Phys. Rev. Lett.* **109**, 115301 (2012).
- [18] X. J. Liu, M. F. Borunda, X. Liu, and J. Sinova, *Phys. Rev. Lett.* **102**, 046402 (2009).
- [19] B. M. Anderson, I. B. Spielman, and G. Juzeliūnas, *Phys. Rev. Lett.* **111**, 125301 (2013).
- [20] B. M. Anderson, G. Juzeliūnas, V. M. Galitski, and I. B. Spielman, *Phys. Rev. Lett.* **108**, 235301 (2012).
- [21] L. W. Cheuk, A. T. Sommer, Z. Hadzibabic, T. Yefsah, W. S. Bakr, and M. W. Zwierlein, *Phys. Rev. Lett.* **109**, 095302 (2012).
- [22] P. J. Wang, Z. Q. Yu, Z. K. Fu, J. Miao, L. H. Huang, S. J. Chai, H. Zhai, and J. Zhang, *Phys. Rev. Lett.* **109**, 095301 (2012).
- [23] Z. H. Lan and P. Öhberg, *Phys. Rev. A* **89**, 023630 (2014).
- [24] C. J. Wang, C. Gao, C. M. Jian, and H. Zhai, *Phys. Rev. Lett.* **105**, 160403 (2010).
- [25] S. Sinha, R. Nath, and L. Santos, *Phys. Rev. Lett.* **107**, 270401 (2011).
- [26] H. Hu, B. Ramachandhran, H. Pu, and X. J. Liu, *Phys. Rev. Lett.* **108**, 010402 (2012).
- [27] Z. Q. Yu, *Phys. Rev. A* **87**, 051606(R) (2013).
- [28] I. A. Bhat, T. Mithun, B. A. Malomed, and K. Porsezian, *Phys. Rev. A* **92**, 063606 (2015).
- [29] Y. Li, X. F. Zhou, and C. J. Wu, *Phys. Rev. A* **93**, 033628 (2016).
- [30] M. Kato, X. F. Zhang, and H. Saito, *Phys. Rev. A* **95**, 043605 (2017).
- [31] M. Kato, X. F. Zhang, and H. Saito, *Phys. Rev. A* **96**, 033613 (2017).
- [32] J. R. Li, J. Lee, W. J. Huang, S. Burchesky, B. Shteynas, F. C. Top, A. O. Jamison, and W. Ketterle, *Nature (London)* **543**, 91 (2017).
- [33] W. Z. Bao and H. Q. Wang, *J. Comput. Phys.* **217**, 612 (2006).
- [34] W. Z. Bao, I. L. Chern, and F. Y. Lim, *J. Comput. Phys.* **219**, 836 (2006).
- [35] W. J. Kwon, S. W. Seo, and Y.-I. Shin, *Phys. Rev. A* **92**, 033613 (2015).
- [36] W. J. Kwon, G. Moon, J.-Y. Choi, S. W. Seo, and Y.-I. Shin, *Phys. Rev. A* **90**, 063627 (2014).

Correction: An NSF grant number was missing in the Acknowledgments and has been inserted.